

A Model-Based Iterative Reconstruction Approach to Tunable Diode Laser Absorption Tomography

Zeeshan Nadir¹, Student Member, IEEE, Michael S. Brown, Mary L. Comer, Senior Member, IEEE, and Charles A. Bouman, Fellow, IEEE

Abstract—Tunable diode laser absorption tomography (TDLAT) has emerged as a popular noninvasive technique for simultaneous sensing of gas concentration and temperature. However, TDLAT imaging of concentration and temperature is an ill-posed, nonlinear inverse problem. Major challenges of TDLAT imaging include a highly nonlinear forward model, few projection measurements, and limited training data. We propose a novel model-based iterative reconstruction (MBIR) framework for TDLAT imaging. To do this, we formulate a nonlinear forward model for TDLAT that incorporates the physics of light absorbance through gaseous media, and we couple it with a non-Gaussian prior model based on a Gaussian mixture distribution that can be trained using a sparse training set. We show that the resulting MAP estimation problem can be solved using majorization minimization together with a novel multigrid optimization algorithm that solves the resulting optimization problem using an orthogonal basis set. Reconstructions using simulated TDLAT datasets show that our TDLAT-MBIR method can reduce reconstruction error while also resulting in a very computationally efficient algorithm.

Index Terms—Gaussian mixture models, GMM, non-convex optimization, non-homogeneous image model, tunable diode laser absorption spectroscopy, tunable diode laser absorption tomography, TDLAS, TDLAT, tomography.

I. INTRODUCTION

SIMULTANEOUS reconstruction of gas flow properties like concentration and temperature is a challenging nonlinear inverse problem [1] and appears in many applications including the monitoring of industrial exhaust [2] and diagnostics of engines [3]–[5]. Among different in situ gas flow diagnostic techniques, tunable diode laser absorption tomography (TDLAT) [6]–[10] has become popular because of its ability

Manuscript received September 1, 2016; revised February 9, 2017; accepted March 18, 2017. Date of publication March 30, 2017; date of current version November 6, 2017. This work was supported in part by the High Speed Systems Test Program at AEDC (Ed Tucker Executing Agent) and in part by the Air Force Office of Scientific Research. The associate editor coordinating the review of this manuscript and approving it for publication Prof. Laura Waller. (*Corresponding author: Zeeshan Nadir.*)

Z. Nadir, M. L. Comer, and C. A. Bouman are with the School of Electrical and Computer Engineering, Purdue University, West Lafayette, IN 47907-2035 USA (e-mail: znadir@purdue.edu; comerm@purdue.edu; bouman@purdue.edu).

M. S. Brown is with the Air Force Research Laboratory, Wright-Patterson AFB, OH 45433 USA (e-mail: michael.brown.191@us.af.mil).

This paper has supplementary downloadable material available at <http://ieeexplore.ieee.org>, provided by the authors. The material includes a pdf file that has the training dataset used in this paper.

Color versions of one or more of the figures in this paper are available online at <http://ieeexplore.ieee.org>.

Digital Object Identifier 10.1109/TCI.2017.2690143

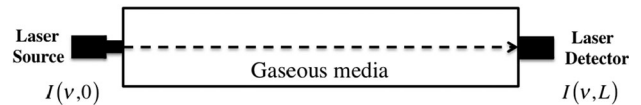


Fig. 1. Illustration of a TDLAT measurement for a single projection path. $I(\nu, 0)$ and $I(\nu, L)$ are the baseline and transmitted light intensity respectively at frequency ν . L is the length of the projection path.

to track rapidly varying signals [11], [12], the high signal-to-noise ratio signals it can produce, and the wide availability of operationally simple tunable diode lasers [13].

Fig. 1 shows an illustration of a TDLAT measurement system for a single projection path. In TDLAT imaging of gases, tunable diode laser sources are employed to emit laser light at particular discrete frequencies [3], [14]. These frequencies correspond to quantum absorption transitions of a particular target molecule [15], [16]. The absorbance of light passed through the gaseous media is measured by using laser light detectors and is then used to reconstruct flow properties. The details of TDLAT measurement systems can be found in [13], [17].

Reconstruction of TDLAT data poses many challenges that make it quite different from traditional tomographic reconstruction of X-ray CT data [18], [19]. First, the TDLAT measurement model is highly nonlinear due to nonlinear dependence of light absorption on temperature. Second, TDLAT imaging systems typically only allow for a small number of projection measurements due to the physical limitations imposed by optical access and short lived combustion phenomenon [17]. For example, in a typical TDLAT system there may be only 10 to 100 measurements available to estimate 1000 to 10 000 pixel unknowns. Therefore, the reconstruction problem is highly ill-posed and nonlinear, so conventional tomographic techniques such as filtered back projection (FBP) [20], [21] are not appropriate.

In order to help constrain the solution, many restrictive assumptions have been used in the past. These include assuming uniform flow properties along the projection path [15], [22], assuming axisymmetric flow [23]–[25] and assuming different flow profiles [26]. However, these assumptions are often inappropriate for many applications that involve non-uniform and high speed turbulent gas flows [14], [17], [27]–[29]. Moreover, these simplistic assumptions do not allow for spatially resolved reconstruction of gas flow properties.

Some of the early studies to obtain spatially resolved gas flow properties without imposing restrictive assumptions were

based upon FBP together with a nonlinear inversion step [8], [11], [30]. However, these approaches require a large number of projection measurements at many different viewing angles (more than 500 projections). M. Ravichandran *et al.* worked on improving the quality of concentration and temperature reconstructions using a finite domain direct inversion (FDDI) method [31] and modified convolution back projection [32], both using more than 100 projections. In [9], a fan beam geometry was used to reconstruct concentration and temperature using a rotatory mechanism to acquire 55 projections at different angles.

Perhaps more closely related methods to our work are the iterative reconstruction methods. For example, in [33] concentration and temperature are reconstructed by solving an optimization problem using 200 projection measurements and L2 regularization, or equivalently, a Gaussian Markov random field prior model. In [34], a principal component analysis (PCA) basis set for the concentration and temperature were used to perform reconstructions using 200 projection measurements. These bases were obtained by using 5000 simulated phantoms for each of the concentration and temperature fields. However, this approach did not take into account the correlation between the concentration and temperature fields. Both [33] and [34] use simulated annealing to solve their corresponding optimization problems which is computationally very expensive as is noted in their results.

An alternate approach to improve the accuracy of tomographic reconstructions is the use of model-based iterative reconstruction (MBIR) methods [35]–[39]. In MBIR, a model is specified for both the measurement process (forward model) and for the unknown image to be reconstructed (prior model). Typically, a maximum a posteriori (MAP) estimate of the unknown image is computed that optimally fits both the forward model and the prior model.

An important benefit of model based methods is that they allow for the incorporation of nonlinear forward models along with prior models that can be trained using representative images. For example, in TDLAT imaging, recently there has been a use of computational fluid dynamics (CFD) simulated images of molecular density and temperature fields which accurately capture the properties of gas flow [13], [40]. These CFD simulated images can potentially be used to improve the reconstruction quality by providing training examples for the prior model [6]. However, CFD simulation images are computationally expensive to compute and therefore usually very few of them are available for training. Moreover, typical CFD images are spatially non-homogeneous and tend to cluster in groups or modes with similar behavior. This makes it difficult to accurately represent them with typical prior models such as Markov random fields (MRF) [41]–[47].

In this paper, we propose a fast MBIR framework that we call TDLAT-MBIR for simultaneous reconstruction of 2-D molecular density and temperature fields of gaseous flow. There are four major contributions of our approach for TDLAT imaging.

- 1) A nonlinear physics-based forward model;
- 2) A Gaussian mixture model (GMM) as the prior model;
- 3) A majorization technique for computing the MAP estimate;

- 4) A multigrid algorithm for solving the required optimization.

Our MBIR approach incorporates a nonlinear forward model of the light absorption through the gaseous media. However, since the number of measurements is so small, we must also incorporate an advanced non-Gaussian prior model that can capture the multivariate distribution of the molecular density/temperature fields. We do this by training a Gaussian mixture model (GMM) to model general non-Gaussian distributions of the combined molecular density and temperature fields. The GMM is particularly useful since it can model the empirical distribution of modes that typically occur in real flow fields.

In order to compute the MAP estimate, we introduce a majorization minimization technique for computing the surrogate cost function for the required optimization. To do this, we present a general theory for the creation of surrogate functions of multivariate mixture distributions that generalizes previous results for scalar Gaussian mixtures [48], [49]. Our final innovation is a multigrid algorithm that uses an orthogonal basis set to find a good solution to the resulting non-convex optimization problem.

Experimental results using simulated TDLAT data generated using CFD phantoms show that our method can produce fast reconstructions of relatively high resolution images (i.e., 45×45) and very few projection measurements (i.e., 40 projection measurements obtained from 10 projection paths and 4 transition frequencies). Results show that the proposed prior model improves the reconstruction quality both visually and quantitatively by accurate modeling of non-homogeneous and non-Gaussian behaviors of the CFD images. Results also indicate that the proposed multigrid algorithm reduces the computation time by speeding convergence.

II. FORMULATION OF MAP COST FUNCTION

A typical approach to model-based inversion is to compute the MAP estimate of the unknown which is given as

$$\hat{x} = \arg \min_x \{ \log p(y|x) + \log p(x) \}, \quad (1)$$

where y is the measurement vector, x is the joint vector of unknown molecular density and temperature, $p(y|x)$ is the probability of observing the data vector y given the unknown x (also called the forward model), and $p(x)$ is the probability of unknown x (also called the prior model).

A. Forward Model

The TDLAT imaging technique yields projection measurements by measuring light absorbance through gaseous media, which in our case is water vapor in the air. Light intensity measurements are made along projection paths and at multiple discrete transition frequencies. Fig. 2 shows the optical projection path layout used in the simulations. Ten optical line of sight (LOS) paths indexed by $j \in \{1, 2, 3, \dots, J\}$, for $J = 10$, are arranged in a rectilinear grid with non-uniform spacing. Laser light is swept over the optical frequency around four discrete transition frequencies indexed by $k \in \{1, 2, \dots, K\}$, for

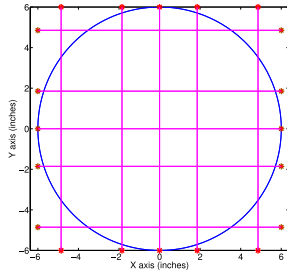


Fig. 2. Schematic of the region of interest and projection measurement paths. The magenta lines show the laser beam paths of the projection measurements. The blue circle represents the boundary of the flowing medium. The red asterisks are the source-detector pairs. The region of interest is inside the blue circle.

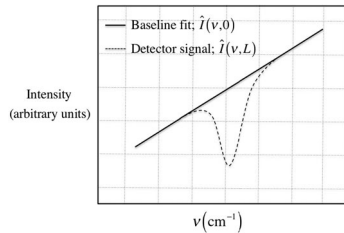


Fig. 3. Illustration of raw light intensity signals. $\hat{I}(\nu, 0)$ and $\hat{I}(\nu, L)$ are the baseline and transmitted measured light intensity respectively at frequency ν . L is the length of the projection path. The laser light is swept in an interval around a particular discrete frequency called the transition frequency.

$K = 4$. For each (j, k) , a projection measurement $Y_{j,k}$ (cm^{-1}) is made

$$Y_{j,k} = \int_{\nu_{1,k}}^{\nu_{2,k}} \ln \frac{\hat{I}(\nu, 0)}{\hat{I}(\nu, L_j)} d\nu, \quad (2)$$

where $\hat{I}(\nu, 0)$ and $\hat{I}(\nu, L_j)$ are the measured baseline and transmitted laser light intensities along the j^{th} path ($\text{watts}\cdot\text{cm}^{-2}$), ν is the optical frequency (cm^{-1}), $[\nu_{1,k}, \nu_{2,k}]$ is the frequency interval of k^{th} absorption transition, and L_j is the length of the j^{th} path (cm). The integral in (2) is typically approximated using a Riemann sum. Fig. 3 shows an example of TDLAT light intensity signals. Appendix A describes the choice of transition frequencies used in this paper.

The forward model for light absorbance measurements is derived using Einstein's theory of radiation [26]. The fractional absorbance of collimated light at frequency ν , when passed through a differential length dr of gas sample is given by

$$dI(\nu, r) = -N(r)S_k(T(r))\phi_k(\nu)I(\nu, r)dr, \quad (3)$$

where r is the position along the laser light path in 2-D space (cm), $I(\nu, r)$ is light intensity, $N(r)$ is the unknown molecular density of the target gas ($\text{molecules}\cdot\text{cm}^{-3}$), $T(r)$ is the unknown temperature of the target gas (Kelvin), ϕ_k is the line shape function (cm) and $S_k(T)$ is the line strength function of the target gas ($\text{cm}^{-1}/(\text{molecules}\cdot\text{cm}^{-2})$). The lineshape function is normalized so that

$$\int_{\nu_{1,k}}^{\nu_{2,k}} \phi_k(\nu) d\nu = 1. \quad (4)$$

The linestrength function $S_k(T)$ [50] is given as

$$S_k(T) = S_k(T_0) \frac{Q(T_0)}{Q(T)} \exp \left[-\frac{hcE_k^l}{k_B} \left(\frac{1}{T} - \frac{1}{T_0} \right) \right] \times \left[\frac{1 - \exp(-hc\nu_k/k_B T)}{1 - \exp(-hc\nu_k/k_B T_0)} \right], \quad (5)$$

where $Q(T)$ is the partition function of the absorbing molecule [50], k_B is the Boltzmann constant, h is Planck's constant, c is the speed of light, E_k^l is the lower state energy level of the k^{th} absorption transition, ν_k is the discrete transition frequency, and T_0 is the reference temperature. The partition function $Q(T)$ is a continuous function of temperature and is specific to the target molecule. Typically the partition function is calculated using a cubic spline polynomial. The estimation of cubic spline polynomial coefficients for the partition function is described in detail in Appendix B.

The absorbance of light follows from (3) by integrating over the projection path,

$$\ln \frac{I(\nu, 0)}{I(\nu, L_j)} = \phi_k(\nu) \int_{\Gamma_j} N(r) S_k(T(r)) dr, \quad (6)$$

$$\int_{\nu_{1,k}}^{\nu_{2,k}} \ln \frac{I(\nu, 0)}{I(\nu, L_j)} d\nu = \int_{\Gamma_j} N(r) S_k(T(r)) dr, \quad (7)$$

where Γ_j is the j^{th} projection path and (7) uses the fact that $\phi_k(\nu)$ is a unit area function. However, in practice the light intensity measurements are noisy due to a variety of noise sources including electronic noise, shot noise, digitization noise, beam steering, light scattering by particles and uncertainty in the spectroscopic database [50]. To incorporate different sources of noise, we model the noise as additive white Gaussian noise with mean 0 and variance σ^2 [33], [34]. Consequently, the projection measurements are related to the light absorbance model by the following equation,

$$Y_{j,k} = \int_{\Gamma_j} N(r)S_k(T(r)) dr + W_{j,k}, \quad (8)$$

$$= \int_{\Gamma_j} f_k(N(r), T(r)) dr + W_{j,k}, \quad (9)$$

where $W_{j,k} \sim \mathcal{N}(0, \sigma^2)$ is additive white Gaussian noise and $f_k(N(r), T(r)) = N(r)S_k(T(r))$ is a function defined for notational convenience.

For 2-D reconstruction of $N(r)$ and $T(r)$, the region of interest is discretized into a grid of $p/2$ square pixels. Let $N = [N_1, N_2, \dots, N_{p/2}]^t$ and $T = [T_1, T_2, \dots, T_{p/2}]^t$ represent the unknown molecular density and temperature vectors and let $x = [N^t T^t]^t \in \mathbb{R}^p$ be the joint vector of unknowns. Equation (9) can then be approximated as

$$Y_{j,k} = \sum_{i=1}^{p/2} H_{j,i} f_k(N_i, T_i) + W_{j,k}, \quad (10)$$

where $H_{j,i}$ is the weighting coefficient for the j^{th} projection path and i^{th} pixel. Writing equation (10) compactly in terms of matrix-vector notation yields

$$Y = H[F(x)] + W, \quad (11)$$

where $Y \in \mathbb{R}^{J \times K}$ are measurements, $H \in \mathbb{R}^{J \times \frac{p}{2}}$ is the forward projection matrix, $F(x) = [f_1(x) f_2(x) \dots f_K(x)] \in \mathbb{R}^{\frac{p}{2} \times K}$, where $f_k(x) = f_k(N, T) \in \mathbb{R}^{\frac{p}{2}}$ are column vectors such that each column $f_k(x)$ represents the function f_k over the entire domain of interest for a particular absorption transition and $W \in \mathbb{R}^{J \times K}$ is the white noise matrix such that $[W]_{j,k} \sim \mathcal{N}(0, \sigma^2)$. Putting this together, the log likelihood of the measurements Y given the unknown x is given by

$$\log p(Y|x) = -\frac{1}{2\sigma^2} \left\| Y - H[F(x)] \right\|_2^2 + \epsilon, \quad (12)$$

where ϵ is a constant that does not depend on x and the norm in equation (12) is the Frobenius norm.

B. Prior Model

We model the joint distribution of the molecular density N and the temperature T using a Gaussian mixture model (GMM) with M mixture components. A major advantage of GMM prior over existing prior models like Markov random fields (MRF) and dictionary learning (DL) methods is that it models the non-homogeneous and the non-Gaussian characteristics of the N and T fields. In contrast, MRFs and DL methods require the images to be modeled as stationary random processes. In this problem, modeling the non-homogeneous behaviors and the long-range correlations between the pixels of N and T are of crucial importance. The GMM prior model implemented in the eigenimage domain allows for these non-Gaussian and non-homogeneous dependencies to be captured effectively and can be trained with a sparse training dataset.

The likelihood function of $x = [N^t T^t]^t$ is given by

$$p(x) = \sum_{m=1}^M \frac{\pi_m |B_m|^{\frac{1}{2}}}{(2\pi)^{\frac{p}{2}}} \exp \left\{ -\frac{1}{2} \|x - \mu_m\|_{B_m}^2 \right\}, \quad (13)$$

where π_m, μ_m represent the prior probability and mean of the mixture component m and B_m represents the precision matrix of mixture component m or equivalently the inverse of the component covariance matrix R_m .

1) *Transformed Representation of x* : While the dimension p of the unknown x can be several thousand, x typically resides on a thin manifold in this higher dimensional space. In order to reduce the dimension of our problem, we will represent the image as

$$x = Ez, \quad (14)$$

where $z \in \mathbb{R}^{\tilde{p}}$ is a lower dimensional representation of the image and E is a $p \times \tilde{p}$ matrix with orthonormal columns. If x has a Gaussian mixture distribution, then it is easily shown that z must also have a Gaussian mixture distribution with parameters given by

$$\tilde{\pi}_m = \pi_m, \quad (15)$$

$$\tilde{\mu}_m = E^t \mu_m, \quad (16)$$

$$\tilde{R}_m = E^t R_m E, \quad (17)$$

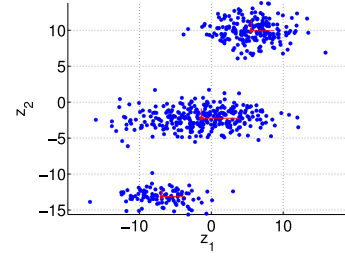


Fig. 4. Illustration of parameter estimation of Gaussian mixture model. The figure shows the 2-D scatter plot of a synthesized training data along with the mixture components using an orthogonal basis set. Blue dots are the training data samples. Red dots are the means of the mixture components. Red line segments show the eigenvectors of component covariance matrices where the lengths of the red line segments correspond to the standard deviation of variables belonging to the particular mixture component.

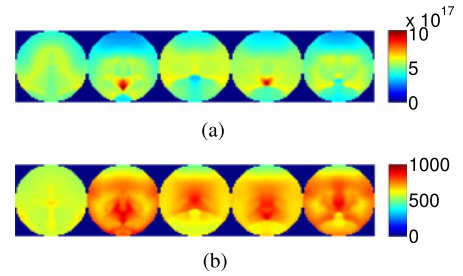


Fig. 5. Example of CFD simulated phantoms. Each phantom consists of a pair of molecular density and temperature image. The first row consists of molecular density images and the second row consists of the corresponding temperature images. (a) Molecular density images (molecules/cm³). (b) Temperature images (K).

where $\tilde{\pi}_m, \tilde{\mu}_m, \tilde{R}_m$ are the prior class probability, class mean, and class covariance of the random vector z that shall be estimated from the data.

In order to avoid over fitting of the training data, we will constrain the covariance matrices \tilde{R}_m to be diagonal. So the transformation, E , must be chosen to diagonalize R_m for each mixture component m . We do this by first clustering the data x into the desired number of mixture components. Next, we hard classify each sample to a mixture component and subtract off the respective component mean from it giving us an approximate sample covariance matrix, \hat{R}_m , for each mixture component. Once this is done, the columns of E can be computed to be the eigenimage vectors of the averaged component covariance matrix formed by

$$\bar{R} = \sum_{m=1}^M \alpha_m \hat{R}_m, \quad (18)$$

where α_m is the number of hard classified samples in mixture component m . Fig. 4 illustrates the effect of this diagonalization procedure for a 2-dimensional vector x with a Gaussian mixture distribution. Notice that using this technique, the coordinate bases are aligned with the axes of the mixture components. Appendix C explains this procedure in greater detail.

2) *Training Procedure*: Next, we used CFD simulated phantoms, shown in Fig. 5, to estimate the parameters $\tilde{\pi}_m, \tilde{\mu}_m, \tilde{R}_m$

of the Gaussian mixture distribution. These training phantoms come in pairs of molecular density and temperature images. The training phantoms of Fig. 5 are representative of the typical CFD phantoms that we used for training the parameters. The complete set of the training phantoms is available in the supplementary material section of this paper. The GMM parameters are estimated using the EM algorithm software of [51] with the input data given by the \tilde{p} dimensional vectors

$$z^{(i)} = E^t x^{(i)}, \quad (19)$$

where $x^{(1)}, \dots, x^{(n)}$ are the n CFD simulated phantom images used to train the model.

In order to improve the accuracy of the model, the EM algorithm is run with a number of constraints that reduce the number of parameters to be estimated. First, the covariance matrices \tilde{R}_m are constrained to be diagonal. This helps in avoiding the over-fitting of the sparse training set. In addition, the diagonal covariance matrices \tilde{R}_m provide a simpler cost function to minimize as compared to the non-diagonal covariance matrices. Second, for all coordinates greater than some value, p_1 , the mean and the variance are constrained to be equal for all mixture components. Typically, p_1 is a small number such as $p_1 = 3$.¹ Lastly, to avoid singularities in estimating the parameters of GMM [52], each class is required to have at least two data samples assigned to it, so that, $\tilde{\pi}_m \geq 2/n$.

The prior likelihood of the unknown expressed in eigenimage basis set E is then given as

$$p(z) = \sum_{m=1}^M \frac{\tilde{\pi}_m |\tilde{B}_m|^{\frac{1}{2}}}{(2\pi)^{\frac{p}{2}}} \exp \left\{ -\frac{1}{2} \|z - \tilde{\mu}_m\|_{\tilde{B}_m}^2 \right\}, \quad (20)$$

where \tilde{B}_m is the inverse of \tilde{R}_m .

C. MAP Cost Function Expression

To derive the MAP cost function in eigenimage basis set E , we first give the MAP cost function in image domain using equation (1) as

$$c(x) = \frac{1}{2\sigma^2} \left\| Y - H[F(x)] \right\|_2^2 - \log \left(\sum_{m=1}^M \frac{\pi_m |B_m|^{\frac{1}{2}}}{(2\pi)^{\frac{p}{2}}} \exp \left\{ -\frac{1}{2} \|x - \mu_m\|_{B_m}^2 \right\} \right), \quad (21)$$

where all the terms not depending on x have been dropped. Next we use the transformation of equation (14) to write the MAP cost function in terms of the eigenimage basis set E as

$$c(z) = \frac{1}{2\sigma^2} \left\| Y - H[F(Ez)] \right\|_2^2 - \log \left(\sum_{m=1}^M \frac{\tilde{\pi}_m |\tilde{B}_m|^{\frac{1}{2}}}{(2\pi)^{\frac{p}{2}}} \exp \left\{ -\frac{1}{2} \|z - \tilde{\mu}_m\|_{\tilde{B}_m}^2 \right\} \right). \quad (22)$$

¹Choosing large values for p_1 will result in over-fitting of the sparse training set as the number of GMM parameters increase as $M \times (2p_1 + 1) - 1$.

Additionally, we will constrain the reconstruction in the image domain inside the physically feasible region to ensure that all molecular density values $N \in \mathbb{R}^{p/2}$ are non-negative and all temperature values $T \in \mathbb{R}^{p/2}$ are greater than or equal to 296 Kelvins. Thus, the TDLAT-MBIR reconstruction is given as follows

$$\hat{z} = \arg \min_{z \in \Omega} c(z), \quad (23)$$

where

$$\Omega = \{z \text{ s.t. } [N^t \ T^t]^t = Ez \ \& \ N \geq 0 \ \& \ T \geq 296\}. \quad (24)$$

The MAP cost function of equation (22) is non-convex because of both the non-convex forward model term and non-convex prior model term.

It may seem appealing to reconstruct the N and T fields in two stages by first reconstructing $f_k(x)$ and then reconstructing N and T [3], [8], [53]. However, this indirect approach typically does not yield good results because it is suboptimal. The Bayesian method models both the non-linear forward model and the joint prior distribution of N and T resulting in a single cost function that captures the synergy between the forward and the prior model. In comparison, the two-stage approach must also have a separate model for the functions $f_k(x)$. Another significant advantage of the Bayesian approach is that we can inform our prior model of N and T by using CFD simulations. It is also noteworthy that the 2-stage approach does not offer any computational advantages.

III. CONSTRUCTION OF SURROGATE COST FUNCTION

The MAP cost function of equation (22) is difficult to minimize since it is non-convex. In particular, the prior model term in the cost function is difficult to minimize directly as it has a mixture of exponentials inside the logarithm. Hence, we simplify the optimization problem by using the majorization minimization technique [18], [54] in which a quadratic surrogate function is used to upper bound the prior term. In order to use the majorization minimization approach, one must find a surrogate function $\hat{c}(z; z')$ such that

$$\hat{c}(z; z') = c(z'), \quad (25)$$

$$\hat{c}(z; z') \geq c(z). \quad (26)$$

We can construct such a surrogate function using the following Lemma [55], [56], proved in Appendix D.

Lemma: Surrogate function for log of exponential mixtures

Let $s : \mathbb{R}^D \rightarrow \mathbb{R}$ be a function which takes the form,

$$s(z) = -\log \left(\sum_m w_m \exp \{-u_m(z)\} \right), \quad (27)$$

where $w_m \in \mathbb{R}^+$, $\sum_m w_m > 0$ and $u_m : \mathbb{R}^D \rightarrow \mathbb{R}$. Furthermore $\forall (z, z') \in \mathbb{R}^D \times \mathbb{R}^D$ define the function

$$G(z; z') \triangleq -s(z') + \sum_m w'_m (u_m(z) - u_m(z')), \quad (28)$$

where $w'_m = \frac{w_m \exp\{-u_m(z')\}}{\sum_j w_j \exp\{-u_j(z')\}}$. Then $\forall (z, z') \in \mathbb{R}^D \times \mathbb{R}^D$, $G(z; z')$ satisfies the following two conditions,

$$G(z'; z') = s(z') \quad (29)$$

$$G(z; z') \geq s(z). \quad (30)$$

The conditions mentioned in (29) and (30) are sufficient to guarantee that $G(z; z')$ is a surrogate function for $s(z)$ and therefore that minimizing $G(z; z')$ must also reduce the function $s(z)$.

Comparing the prior log likelihood term in the MAP cost function of equation (22) with the function of equation (27), we define a quadratic surrogate function for the prior log likelihood term,

$$g(z; z') = -\log p(z') + \sum_m \frac{d_m}{2} \left(\|z - \tilde{\mu}_m\|_{\tilde{B}_m}^2 - \|z' - \tilde{\mu}_m\|_{\tilde{B}_m}^2 \right), \quad (31)$$

where

$$d_m = \frac{\tilde{\pi}_m |\tilde{B}_m|^{\frac{1}{2}} \exp\left\{-\frac{1}{2}\|z' - \tilde{\mu}_m\|_{\tilde{B}_m}^2\right\}}{\sum_j \tilde{\pi}_j |\tilde{B}_j|^{\frac{1}{2}} \exp\left\{-\frac{1}{2}\|z' - \tilde{\mu}_j\|_{\tilde{B}_j}^2\right\}}, \quad (32)$$

and z' is the current state of the unknown. The resulting surrogate function for the MAP cost function $c(z)$ is then given by

$$\hat{c}(z; z') = \frac{1}{2\sigma^2} \|Y - H[F(Ez)]\|_2^2 - \log p(z') + \sum_m \frac{d_m}{2} \left(\|z - \tilde{\mu}_m\|_{\tilde{B}_m}^2 - \|z' - \tilde{\mu}_m\|_{\tilde{B}_m}^2 \right). \quad (33)$$

Since our goal is to minimize the cost with respect to z , we may drop the terms involving z' to obtain an equivalent surrogate function given by

$$c(z; z') = \frac{1}{2\sigma^2} \|Y - H[F(Ez)]\|_2^2 + \frac{1}{2} \|z - \tilde{\mu}\|_{\tilde{B}}^2, \quad (34)$$

where

$$\tilde{B} = \sum_{m=1}^M d_m \tilde{B}_m, \quad (35)$$

and

$$\tilde{\mu} = \tilde{B}^{-1} \left(\sum_{m=1}^M d_m \tilde{B}_m \tilde{\mu}_m \right). \quad (36)$$

A typical example of a surrogate function for the prior term is shown for the case of a single coordinate in Fig. 6. The surrogate function has been constructed for a Gaussian mixture prior that has five mixture components and it is plotted for a single coordinate. Notice that in Fig. 6, while the original function corresponding to the GMM prior term is non-convex, the surrogate function is a convex function that forms an upper bound to the original function. It should be noted that the surrogate function of equation (34) is still a non-convex function due to the non-convex forward model term.

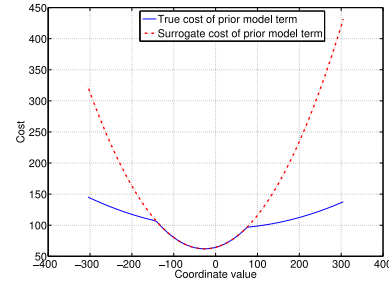


Fig. 6. Example of a surrogate function w.r.t. a single coordinate for GMM prior term with $M = 5$ classes. The blue curve is the cost of the GMM prior term and red curve is the surrogate cost for GMM prior term. The current value of the coordinate is 0.

IV. OPTIMIZATION

In this section, we shall present a multigrid optimization algorithm to solve the MAP estimation problem. We shall also present a fixed-grid algorithm for comparison. Both the multigrid and the fixed-grid algorithms are designed to achieve a local minimum of the non-convex MAP estimation problem of equation (23). The multigrid algorithm, however, has much faster convergence as compared to the fixed-grid algorithm.

Multigrid algorithms can reduce the computational complexity of numerical problems by working on the data at different scales or grids. Multigrid algorithms have been used in many different applications including optical flow estimation [57], [58], signal/image smoothing [59], [60], image segmentation [61], interpolation of missing image data [62], and optical diffusion tomography [63], [64]. The main novelty in our multigrid algorithm is that we introduce a notion of grids using eigenimage basis functions.

Intuitively, the first few eigenimages are spatially smooth, whereas the later ones have more spatial variation. We exploit this by cumulatively increasing the number of eigenimages as we move from coarse to fine grids. We start working on coarse grids first, gradually moving to finer grids, reducing the cost at each grid. This improves the convergence of the multigrid algorithm when compared with the fixed-grid algorithm.

A. Coordinate Update Method

The multigrid and fixed-grid algorithms both work by iteratively minimizing the cost function of equation (22) over individual coordinates z_i but with important differences. Both algorithms use the surrogate function formulation of equation (34) to reduce the 1-D cost. The cost function of equation (34) written as a function of the i^{th} coordinate only is given as,

$$c(z_i; z') = \frac{1}{2\sigma^2} \|y - HF[Ez' + E_{*,i}(z_i - z'_i)]\|_2^2 + \frac{1}{2} (z_i - \tilde{\mu}_i)^2 \tilde{B}_{i,i}, \quad (37)$$

where z' is the current value of the unknown and $E_{*,i} \in \mathbb{R}^{p \times 1}$ is the i^{th} eigenimage.

To reduce this 1-D cost function, we propose a fast and robust coordinate update method. We fit a quadratic

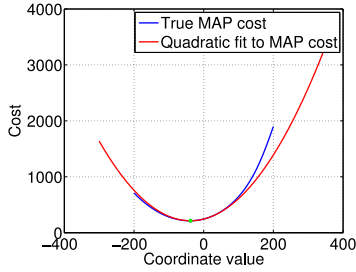


Fig. 7. Illustration of quadratic fit to the 1-D cost function. Current value of coordinate is 0. The green asterisk represents the minima of the true cost as well as the minima of the quadratic fit to the true cost.

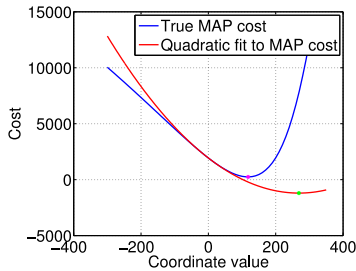


Fig. 8. Example of coordinate update using Brent's method. Current value of coordinate is 0. Green asterisk is the minima of the quadratic fit and magenta asterisk is the minima returned by Brent's method.

function through the 1-D cost function by selecting three points, $(z_i - \epsilon_i, z_i, z_i + \epsilon_i)$ and minimize this quadratic. We choose the step size ϵ_i for each coordinate in an adaptive manner corresponding to the variation in the coordinate;

$$\epsilon_i \leftarrow \delta \sqrt{\tilde{R}(i, i)}, \quad (38)$$

where \tilde{R} is the inverse of the equivalent precision matrix in equation (35) and δ is usually picked between 10^{-5} to 10^{-3} . This procedure is known as inverse parabolic interpolation [65]. A typical example of the quadratic fit is shown in Fig. 7.

The quadratic fit to the true cost function is not necessarily a strict upper bound to the true cost function as shown in Fig. 7, therefore we must check if the true cost is reduced as a result of minimizing the quadratic fit. In rare cases, the true cost could increase, so then we revert to Brent's method that alternates between golden section iterations and quadratic fits [65]. Fig. 8 shows an example where Brent's method is used to reduce the 1-D cost function. The pseudocode of 1-D optimization is given in Fig. 9. The pseudocode of Brent's method can be found in [65].

Finally, at each coordinate update, we ensure that the reconstruction z remains inside the physically feasible region Ω . If after a coordinate update, the reconstruction in the image domain goes out of the feasible region, we project it onto the boundary of the feasible region by changing the value of eigenimage coordinate using a bisection method. More precisely, we iteratively bisect the interval between the optimum value and the old value of the eigenimage coordinate until we satisfy the

```

1: function [ $\hat{u}$ ]  $\leftarrow$  COORDINATEUPDATE( $u'$ ,  $c$ ,  $\epsilon$ )
2: /* Inputs: Initial value of coordinate  $u'$ , Step size  $\epsilon$ , Pointer to cost function of eq. (37)  $c$  */
3: /* Output: Updated value of coordinate  $\hat{u}$  */
4:   Fit a quadratic  $q(u)$  to the cost function in eq. (37) using three points  $(u' - \epsilon, u', u' + \epsilon)$ 
5:    $v \leftarrow \arg \min_u q(u)$ 
6:   if  $c(v) < c(u')$  then
7:      $\hat{u} \leftarrow v$ 
8:   else  $\hat{u} \leftarrow$  Brent ( $u'$ ,  $c$ )
9:   end if
10: end function

```

Fig. 9. Pseudocode of 1-D coordinate update algorithm.

```

1: function [ $\hat{z}$ ]  $\leftarrow$  FIXEDGRID( $y$ ,  $z'$ ,  $\tilde{p}$ )
2: /* Inputs: Measurements  $y$ , Initial condition  $z'$ , Total no. of eigenimage basis vectors  $\tilde{p}$  */
3: /* Output: MAP estimate  $\hat{z}$  */
4:    $\hat{z} \leftarrow z'$ 
5:   while Stopping criterion is not met do
6:     for  $i = 1$  to  $\tilde{p}$  do
7:       Compute  $\tilde{B}$  and  $\tilde{\mu}$  using eq. (32), (35), (36)
8:        $\hat{z}_i \leftarrow \arg \min_{z_i \text{ s.t. } z \in \Omega} c(z_i; z')$   $\triangleright$  Reduce cost of eq. (37)
9:        $z'_i \leftarrow \hat{z}_i$   $\triangleright$  Update the current state
10:    end for
11:  end while
12: end function

```

Fig. 10. Pseudocode of fixed-grid algorithm.

physical feasibility constraints, while at the same time achieving the minimum 1-D cost under these constraints.

B. Fixed-Grid Optimization

In the fixed-grid algorithm, we reduce the cost function on a single grid that consists of all the eigenimage basis vectors. To minimize the cost function, we use the ICD update strategy [66]. ICD, which is related to Gauss-Seidel method and has been found to be suitable for CT applications [67], works by optimizing over each coordinate one by one until some stopping criterion is met. Fig. 10 shows the pseudocode of fixed-grid algorithm.

C. Multigrid Optimization

In the multigrid algorithm, we work at different grids having a different number of eigenimages to be optimized over. At the coarsest grid, we start from the first column vector, $E_{*,1}$, of the eigenimage basis set E and optimize over it. Next, as we move to the fine grids, we increase the number of eigenimages by a factor of ρ at each grid until we include the final eigenimage, $E_{*,\tilde{p}}$, at the finest grid. At each grid, we optimize over a fixed number of eigenimages. This process is repeated in a loop until the stopping condition is met. The pseudocode of multigrid optimization algorithm is presented in Fig. 11 and the coordinate update pattern of the multigrid algorithm is shown in Fig. 12.

V. EXPERIMENTAL RESULTS

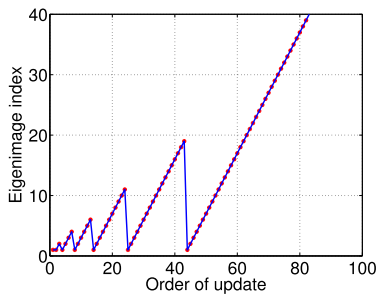
We now present our TDLAT-MBIR image reconstruction results by performing reconstructions of a simulated TDLAT

```

1: function  $[\hat{z}] \leftarrow \text{MULTIGRID}(y, z', G, \rho)$ 
2: /* Inputs: Measurements  $y$ , Initial condition  $z'$ , Total number of grids
    $G$ , Factor for calculating grid coefficients  $\rho$  */
3: /* Output: MAP estimate  $\hat{z}$  */
4:  $\hat{z} \leftarrow z'$ 
5: while Stopping criterion is not met do
6:   for  $j = 0$  to  $G - 1$  do                                ▷ For each grid level
7:     for  $i = 1$  to  $\rho^j$  do
8:       Compute  $\tilde{B}$  and  $\tilde{\mu}$  using eq. (32), (35), (36)
9:        $\hat{z}_i \leftarrow \arg \min_{z_i \text{ s.t. } z \in \Omega} c(z_i; z')$   ▷ Reduce cost of eq. (37)
10:       $z'_i \leftarrow \hat{z}_i$                                 ▷ Update the current state
11:     end for
12:   end for
13: end while
14: end function

```

Fig. 11. Pseudocode of multigrid algorithm.

Fig. 12. Coordinate update pattern in one full iteration of Multigrid algorithm using $\rho = 1.8$ and $\tilde{p} = 40$.

dataset. To test our proposed Gaussian mixture prior model and multigrid optimization algorithm, we perform reconstructions on CFD simulated phantoms. These CFD phantoms are obtained by running simulations for a single axial plane of an engine having a diameter of 12 inches. The CFD simulated phantoms are used to produce simulated projection measurement data using the measurement layout of Fig. 2. This simulated measurement dataset is then used in all the experiments.

First, we compare the reconstruction results of the proposed prior model with the results of two different prior models; Gaussian model (GM) [6] and Gaussian Markov random field (GMRF) model [41] and also with the reconstruction results of the proper orthogonal decomposition (POD) approach of [34].² We compare the reconstructions both visually and using an objective criterion of normalized root mean squared error (NRMSE). The NRMSE between two images X and Z is defined as

$$\text{NRMSE}(X, Z) = \frac{\sqrt{\frac{1}{n} \sum_{i=1}^n (X_i - Z_i)^2}}{\max_i(Z_i) - \min_i(Z_i)}. \quad (39)$$

We provide some reconstruction results for visual comparison and also provide a table that shows the average results of all the reconstructions.

²Our implementation of POD approach is similar to [34], however, unlike [34], we do not use the simulated annealing algorithm. We use our proposed multigrid algorithm of Fig. 11 without imposing any bounds on the eigenimage coordinate values.

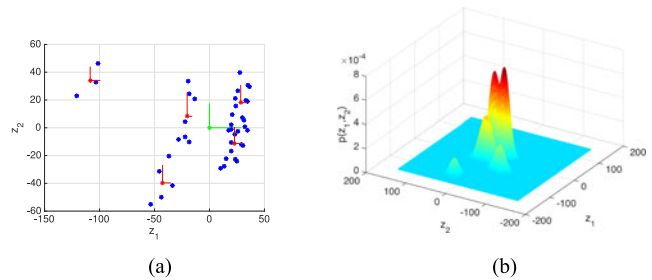


Fig. 13. Illustration showing the multi-modal nature of the distribution of the CFD training data. (a) Shows the scatter plot of the CFD training data expressed in eigenimages. The blue dots are the data samples and the red dots are the means of the estimated Gaussian mixture components. The green dot represents mean of estimated Gaussian distribution. The length of the red and green segments corresponds to the standard deviation of the corresponding eigenimage coordinates. (b) Shows the mesh plot of probability density function of Gaussian mixture model.

Finally, we perform convergence experiments to compare our multigrid optimization algorithm with conventional fixed-grid optimization algorithm. We compare the speed of convergence using two different metrics. One of them is the MAP cost, whereas the other is the normalized root mean squared error (NRMSE) between the current state and the converged state of the unknown fields N and T . We present the plots of MAP cost and NRMSE between current and converged state of the unknown fields N and T .

A. Comparison of Reconstruction Results

To test our proposed GMM prior model, we perform reconstruction experiments using CFD simulated phantoms. A total of 42 CFD phantoms are available, so we perform 42 reconstruction experiments, where in each experiment, we keep one phantom for testing and train the prior model on the rest of the 41 phantoms. The image array size in the reconstructions is kept at 45×45 ; however, since the region of interest is a circle, the total number of unknowns $p = 3194$. The TDLAT measurements are simulated using (12) with an average SNR of 30 dB. This corresponds to a value of noise standard deviation σ , which is roughly 3% of the mean value of forward projections representing practical scenarios. Also, for these simulations $J = 10$ and $K = 4$, so $Y \in \mathbb{R}^{10 \times 4}$.

We set $M = 5$ and $p_1 = 3$, since we found that using these values in the experiments yielded the lowest average NRMSE results. We estimate the parameters of the mixture model in the eigenimage basis space E using expectation-maximization algorithm. We constrain the mixture component covariance matrices \tilde{R}_m to be diagonal.

Fig. 13(a) shows the scatter plot of the training data using eigenimage basis domain. In this figure, the blue dots represent the training data, the red dots represent the means of the different mixture components when the data is modeled using GMM, while the green dot represents the mean of the data when modeled using Gaussian distribution. It is clear from this figure that the CFD data exhibits a multi modal distribution which is captured by using a Gaussian mixture model as the prior

TABLE I
AVERAGE NRMSE FOR ALL 42 RECONSTRUCTION EXPERIMENTS.

	% NRMSE (N)	% NRMSE (T)	% Avg. NRMSE
POD	9.89	12.13	11.01
GMRF	10.00	13.50	11.75
GM	6.15	5.51	5.83
GMM	6.14	5.14	5.64

NRMSE(N) is Average NRMSE in Molecular Density. NRMSE(T) is Average NRMSE in Temperature. Avg. NRMSE is Average of the NRMSE in Molecular Density and Temperature

distribution. Modeling this data using a Gaussian distribution does not capture different empirical modes evident in the scatter plot. Fig. 13(b) shows the probability density function of the Gaussian mixture model whose parameters are trained from the CFD training data.

For all the experiments, the initial condition for GMRF reconstructions is a constant image for both the N and T fields, the initial condition for GM and POD reconstructions is the mean of the training data, and the initial condition for GMM reconstruction is the end result of GM reconstruction. The initial conditions were chosen in an effort to achieve lowest possible final value of MAP cost function after convergence of the optimization procedure. The regularization level was chosen for GMRF, GM, and GMM to achieve the lowest NRMSE, whereas in POD there is no regularization parameter to be set.

For POD, GM, and GMM reconstructions, we run 3 iterations of multigrid optimization algorithm using the eigenimage basis as described in Section IV. The coarsest grid has only 1 eigenimage coefficient, the finest grid has 40 and $\rho = 1.8$. For the GMRF reconstructions, we use a multi-resolution approach by performing reconstructions on three different scales, where, at each finer scale, we use the end result of the next coarser scale as an initial condition.

Table I shows NRMSE results averaged over all 42 reconstructions. It is evident that overall the GMM prior gives the lowest NRMSE results. The GMRF prior model gives the highest NRMSE results. This could be because the GMRF is not a very expressive prior model particularly for CFD phantoms; and with a sparse measurement set, the prior serves an important role in avoiding the estimation of a reconstruction that is unlikely to occur.

It appears from the reconstructed example results in Figs. 15 and 16 that the GMM prior model and the GM prior model produce the best reconstruction results, however, only the reconstructions with the GMM prior model capture the dense patches in the molecular density fields. The POD technique gives false dense patches in the molecular density reconstructions. This might be because the POD technique does not model the correlation between concentration and temperature. Although smooth, the GMRF reconstructions fail to capture the essential structure in N and T fields. It seems that with the very sparse measurement set, GMRF tends to overly smooth the reconstructions.

We also studied the effect of changing the number of Gaussian mixture components M in GMM prior model. With 41 CFD phantoms available for training, we found out that $M = 5$

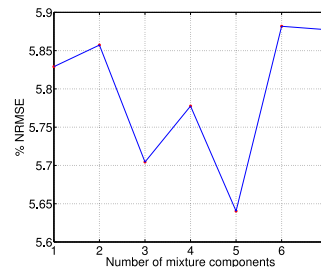


Fig. 14. Plot of % average NRMSE vs. no. of mixture components in Gaussian mixture prior model. Average NRMSE is the average of NRMSE in molecular density and temperature reconstructions.

mixture components gave us the best results. Fig. 14 shows the average NRMSE of 42 reconstructions as a function of the number of mixture components.

B. Convergence Results

We compared the convergence speed of our multigrid optimization algorithm with our fixed-grid optimization algorithm by running 42 reconstruction experiments using a Gaussian mixture prior model. The initial condition for these reconstructions is the end result of reconstructions with the Gaussian prior model. For each reconstruction, we first run the algorithm for a sufficiently large number of iterations to achieve a “fully converged” result. We then run the same reconstructions again and at each coordinate update we compute the MAP cost and the NRMSE between the current and the converged state of the unknown fields N and T . Both multigrid and fixed-grid algorithms use eigenimage bases. In the case of the multigrid algorithm, the coarsest grid has 1 eigenimage coordinate, the finest grid has 40 eigenimage coordinates and $\rho = 1.8$.

Fig. 17(a) shows a comparison of cost plots averaged over 42 reconstructions. It is evident that the cost drops much more quickly with the multigrid algorithm. This makes sense since the multigrid algorithm spends more computation on eigenimage coefficients which are expected to have more variation in the eigenimage domain.

In Fig. 17(b) and 17(c) we present % NRMSE plots between current and converged state of the unknown molecular density and temperature fields averaged over 42 reconstructions. It is clear from the figures that the multigrid algorithm converges much faster than the fixed-grid algorithm. Typically for these reconstructions, a 1% NRMSE criterion is enough to guarantee sufficient convergence. In Fig. 18, we observe the speed-up as a function of % NRMSE between the current and converged result. We define the speed-up as

$$\text{speed-up } (r) = \frac{\text{Average fixed-grid iterations to achieve } r \% \text{ NRMSE}}{\text{Average multigrid iterations to achieve } r \% \text{ NRMSE}}. \quad (40)$$

Hence speed-up at r % NRMSE would be the relative decrease in the computation that one gets by using the multigrid algorithm as opposed to the fixed-grid algorithm to achieve an

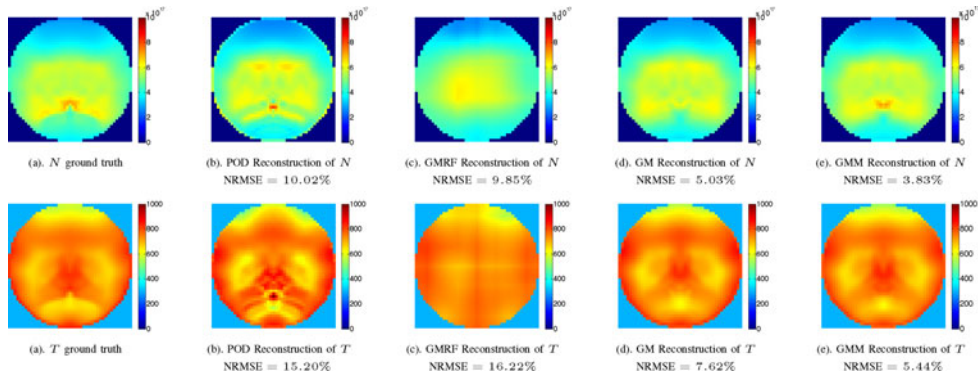


Fig. 15. Example 1 of TDLAT reconstructions. The scale of N is 0 to 10×10^{17} molecules- cm^{-3} and the scale of T is 0 to 1000 Kelvins. Both GM and GMM produce good reconstruction results, however, GMM captures the dense region in molecular density reconstruction, whereas, GM does not. POD seems to suffer from a lot of artifacts, whereas, GMRF seems to overly blur the details.

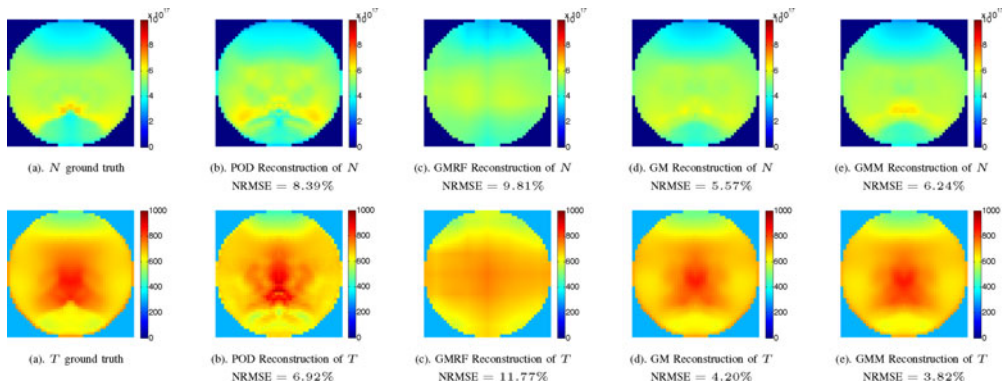


Fig. 16. Example 2 of TDLAT reconstructions. The scale of N is 0 to 10×10^{17} molecules- cm^{-3} and the scale of T is 0 to 1000 Kelvins. Both GM and GMM produce good reconstruction results, however, GMM captures the dense region in molecular density reconstruction, whereas, GM does not. POD seems to suffer from a lot of artifacts, whereas, GMRF seems to overly blur the details.

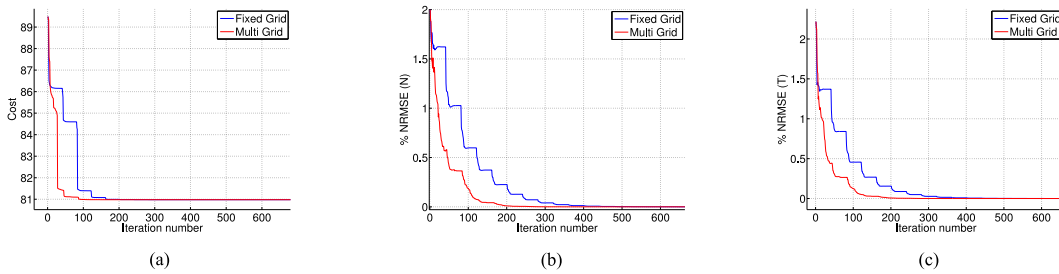


Fig. 17. Comparison of convergence speed of fixed-grid and multigrid algorithm. All three plots represent an average from 42 reconstructions. These plots are representative of the typical behavior. It can be seen from all three plots that multigrid algorithm converges faster than fixed-grid algorithm. (a) MAP cost plot. (b) %NRMSE between current and converged value of N . (c) %NRMSE between current and converged value of T .

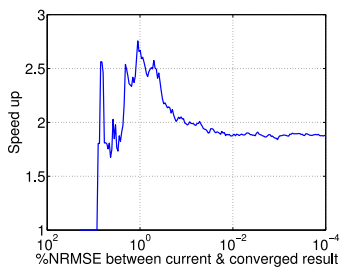


Fig. 18. Average relative decrease in computational time when using the multigrid algorithm as opposed to fixed-grid algorithm. To achieve a 1 % NRMSE between the current and the covered result, multigrid algorithm requires about 0.27 seconds, whereas fixed-grid algorithm requires about 0.73 seconds on a computer with an Intel core i7 processor and 32 GB memory using MATLAB.

NRMSE of r % in both N and T fields. It is clear from Fig. 18 that the multigrid algorithm is almost uniformly better than the fixed-grid algorithm. The speed-up seems to converge at about a factor of 1.8 for very conservative criterion of NRMSE, whereas for a more practical convergence criterion i.e., 1 % NRMSE, there is a speed-up factor of 2.7.

VI. CONCLUSION

We have proposed a novel framework that we have named TDLAT-MBIR for reconstruction of TDLAT dataset. We first derived a forward model based upon physics of light absorbance through gaseous media. Next, we proposed a Gaus-

TABLE II
ABSORPTION SPECTROSCOPIC LINE PARAMETERS

Transition Frequency ν_k (cm^{-1})	Lower Energy State E_k^l (cm^{-1})
7181.156	136.762
7161.410	224.838
7185.597	1045.058
7179.752	1216.195

sian mixture model as a prior model for images that can capture non-homogeneous and multimodal behaviors of the image distributions. We presented a methodology for training the parameters of this model. Finally, we proposed a multigrid optimization algorithm using eigenimage basis functions along with a robust 1-D optimization strategy. Reconstruction results using CFD simulated phantoms indicate that the proposed GMM prior model improves the quality of reconstructions and the multigrid optimization algorithm improves convergence.

APPENDIX A

SELECTION OF ABSORPTION LINE SPECTRUM

In hyperspectral TDLAT, more than a single absorption line spectrum, typically more than two, are analyzed to collect data [33]. This increases the information content by adding more measurements at different discrete optical frequencies. This is important to offset the very low number of LOS projection measurement paths. There are many factors that determine the absorption lines to be chosen. For example, strength of absorption, spectral separation between absorption lines, temperature sensitivity of absorption lines, effects of boundary layers and lack of interference from nearby absorption lines [16]. Other factors that affect the selection of lines include expected sensor operating conditions and hardware capabilities [22].

In this paper, we are using water as our target molecule because of its natural availability as a major combustion product, strong rovibrational transitions [13] and wide range of transition frequencies. Therefore, the transition frequencies are chosen according to the properties of the water molecule. The four different absorption transition lines that are used in this work are given in Table II. These absorption transition lines are same as the ones used in [40].

APPENDIX B

ESTIMATION OF SPLINE COEFFICIENTS FOR Q FUNCTION

The partition function $Q(T)$ acts as a normalizing constant for the probability of occupation of a particular quantum state at temperature T [68]. In practice, even for simple molecules like H_2O , the partition function is difficult to calculate. Typically, the partition function is approximated using cubic spline polynomials which are fit to laboratory derived values that are usually very accurate [16].³ In this study, we used the calculations of the partition function for water done by Gamache *et al.* [68]. We fit cubic splines to the data to get a smooth, twice differentiable curve as seen in Figs. 19, 20(a) and (b).

³We estimated the cubic spline polynomial coefficients to get a partition function $Q(T)$ that is twice differentiable upto 64-bit double precision.

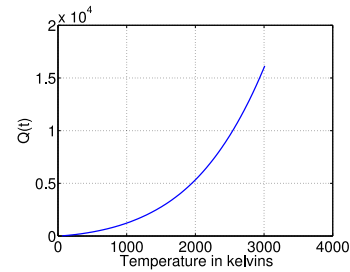


Fig. 19. Plot of partition function using cubic spline polynomial approximation.

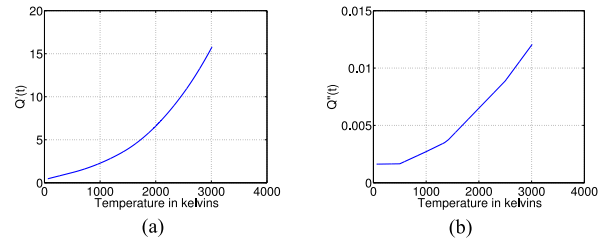


Fig. 20. Derivatives of partition function calculated using cubic spline polynomial approximation. (a) First derivative of Q function. (b) Second derivative of Q function.

The original cubic spline polynomial coefficients, that were made available to us to approximate the partition function were such that the resulting fit was not twice differentiable. Table III shows the cubic spline polynomial coefficients that were provided to us in the beginning. To understand the role of each of the coefficients in the provided tables, we provide the representation of the partition function in a temperature range from T_0 to T_1 ,

$$Q(T) = a + bT + cT^2 + dT^3, \quad T_0 \leq T < T_1. \quad (41)$$

Using the coefficients in Table III, the resulting first and second derivatives are discontinuous at temperature values where a change of polynomial occurs. In order to ensure that the approximated partition function is twice differentiable, we corrected the value of the polynomial coefficients given in Table III and also minimized the overall error using the tabulated values of partition function made available by R. R. Gamache [68]. Following were the steps that were taken to ensure that the resulting cubic spline polynomial coefficients give a twice differentiable curve.

- 1) We ensure the continuity of the second derivative by adjusting the value of coefficient c such that on points where the change of polynomial occurs, the difference in the values of $Q''(T)$ is 0.
- 2) We adjust the values of coefficient b such that on points where the change of polynomial occurs, the difference in the values of $Q'(T)$ is 0. This ensures the continuity of the first derivative of Q function.
- 3) We adjust the values of coefficient a such that on the points where change of polynomial occurs, the difference in the values of $Q(T)$ is 0. This gives us a continuous Q function.

The above procedure gives us a continuous, twice differentiable Q function. Finally, to reduce the overall error between

TABLE III
CUBIC SPLINE COEFFICIENTS FOR Q FUNCTION PROVIDED IN THE BEGINNING

Temp. Range	a	b	c	d
$T < 500$	-18.221850000000000	0.423075200000000	7.703331000000000e-4	6.185911000000000e-9
$500 \leq T < 1000$	-65.944149999999993	0.694548700000000	2.468324000000000e-4	3.484234000000000e-7
$1000 \leq T < 1350$	-61.853600000000000	0.697335600000000	2.183351000000000e-4	3.699410000000000e-7
$1350 \leq T < 1425$	1.166381815424874e5	-2.511038212392546e2	-6.640078900000056e-4	5.878034666666681e-7
$1425 \leq T < 2500$	-1.311914000000000e3	3.214013000000000	-0.001522213000000	7.885532000000000e-7
$2500 \leq T < 5000$	-4.529464000000000e3	7.314166000000000	-0.003265189000000	1.035648000000000e-6

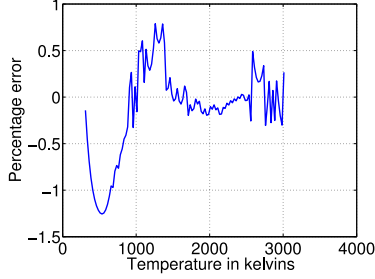


Fig. 21. Plot of percent error in Q function.

experimentally determined values of Q function and the computed values of Q function using the cubic splines, we fit a cubic function to the error and adjust the coefficients a, b, c and d to reduce the error. The error for our final cubic spline fit was below 2% for a range of temperature values given by 300 Kelvin to 3010 Kelvin as shown in Fig. 21. The final cubic spline coefficients that give a continuous, twice differentiable Q function are provided in Table IV.

APPENDIX C

ORTHONORMAL BASIS ESTIMATION PROCEDURE

Let $x^{(1)}, \dots, x^{(n)}$ be the CFD training vectors, where each $x^{(i)}$ is a p dimensional vector. Without any loss of generality, assume that the mean of all the training vectors is 0. Let X be the $p \times n$ training matrix containing all the training images given by

$$X = [x^{(1)}, \dots, x^{(n)}]. \quad (42)$$

We can write the SVD of the matrix X as

$$X = E_1 \Sigma_1 V_1^t, \quad (43)$$

where E_1, Σ_1, V_1 are the left-singular vectors, singular values and right-singular vectors of X . We assume that the singular values are ordered in descending magnitude along the diagonal of the matrix Σ_1 .

We need to obtain an orthonormal basis set E that diagonalizes the class covariance matrices for all the mixture components. We obtain this basis set by applying a rotation transform on E_1 . The need of rotation arises from the fact that E_1 computed through SVD ignores the possibility of different mixture components in the distribution of unknown x .

First we represent the CFD data in eigenimage basis set E_1 as vectors $z^{(1)}, \dots, z^{(n)}$ and estimate the mixture parameters

$\{\pi'_m, \mu'_m, R'_m\}_{m=1}^M$. Next, we bring each mixture component onto the origin by subtracting the component mean off from every data sample. We do this by performing a maximum a posteriori classification of each of the data samples to a mixture component. So let c_i be the MAP classified mixture component of the i^{th} data sample, so,

$$c_i = \arg \max_{1 \leq m \leq M} p(z^{(i)} \text{ belongs to } m^{\text{th}} \text{ component} | z^{(i)}). \quad (44)$$

Let Z' be the matrix in which each column consists of a training data sample after subtracting off the component mean, so,

$$Z' = [z^{(1)} - \mu'_{c_1}, \dots, z^{(n)} - \mu'_{c_n}]. \quad (45)$$

Since we constrain all the mixture components to have a common mean and covariance for all coordinates greater than p_1 , we only need to rotate the first p_1 coordinates of the data samples. Therefore, let Z'' be the matrix that consists of first p_1 rows of Z' . The rotation $E_2 \in \mathbb{R}^{p_1 \times p_1}$ that rotates the first p_1 coordinates of the data samples is computed by performing an SVD decomposition on Z'' ,

$$Z'' = E_2 \Sigma_2 V_2^t. \quad (46)$$

Finally the rotation transform that aligns the GMM components with eigenimage vectors is given as

$$E_3 = \begin{bmatrix} E_2 & 0 \\ 0 & I_{\tilde{p}-p_1} \end{bmatrix} \in \mathbb{R}^{\tilde{p} \times \tilde{p}}, \quad (47)$$

where $I_{\tilde{p}-p_1}$ is an $(\tilde{p} - p_1) \times (\tilde{p} - p_1)$ identity matrix. After obtaining the rotation transform, we recompute the new eigenimage basis vectors set E as

$$E = E_1 \times E_3. \quad (48)$$

APPENDIX D PROOF OF LEMMA

$$\begin{aligned} \log p(x) &= \log p(x') + \log \left(\frac{p(x)}{p(x')} \right) \\ &= \log p(x') + \log \left(\frac{1}{p(x')} \sum_i w_i \exp\{-u_i(x)\} \right) \end{aligned}$$

TABLE IV
ESTIMATED CUBIC SPLINE COEFFICIENTS THAT PRODUCE TWICE DIFFERENTIABLE Q FUNCTION

Temp. Range	a	b	c	d
$T < 500$	-5.108576477504222	0.366653379513569	8.102612279372126e-4	1.056101563185623e-8
$500 \leq T < 1000$	-47.888262602504270	0.623331496263569	2.969049944372127e-4	3.527985046318561e-7
$1000 \leq T < 1350$	-69.405862602503561	0.687884296263569	2.323521944372125e-4	3.743161046318561e-7
$1350 \leq T < 1425$	-6.054292290275050e2	1.879047332763572	-6.499907955627895e-4	5.921785712985233e-7
$1425 \leq T < 2500$	-1.186326812858752e3	3.101989614513568	-0.001508195905563	7.929283046318561e-7
$2500 \leq T < 5000$	-5.047183062858760e3	7.735017114513572	-0.003361406905563	1.040023104631856e-6

$$\begin{aligned}
&= \log p(x') + \log \left(\frac{\sum_i w_i \exp\{-u_i(x)\}}{\sum_j w_j \exp\{-u_j(x')\}} \right) \\
&= \log p(x') + \log \left(\sum_i \frac{w_i \exp\{-u_i(x')\}}{\sum_j w_j \exp\{-u_j(x')\}} \right. \\
&\quad \left. \times \exp\{-u_i(x) + u_i(x')\} \right) \\
&= \log p(x') + \log \left(\sum_i \tilde{\pi}_i \times \exp\{-u_i(x) + u_i(x')\} \right) \\
&\geq \log p(x') + \sum_i \tilde{\pi}_i \times \{-u_i(x) + u_i(x')\}
\end{aligned}$$

We have used Jensen's inequality to derive the result in the last inequality. Multiplying by -1 on both sides of the last inequality results in the expression

$$\begin{aligned}
-\log p(x) &\leq -\log p(x') + \sum_i \tilde{\pi}_i \times \{u_i(x) - u_i(x')\} \\
&= G(x; x').
\end{aligned}$$

Finally if we put $x = x'$, this results in $-\log p(x') = G(x'; x')$.

ACKNOWLEDGMENT

The authors would like to thank Dr. Mark Hagenmaier of the Air Force Research Laboratory, Wright-Patterson AFB, OH for use of the CFD solutions.

REFERENCES

- [1] A. C. Eckbreth, *Laser Diagnostics for Combustion Temperature and Species*, vol. 3. Boca Raton, FL, USA: CRC Press, 1996.
- [2] R. Grisar, *Monitoring of Gaseous Pollutants by Tunable Diode Lasers*. Hingham, MA, USA: Reidel, 1988.
- [3] J. Li, Z. Du, T. Zhou, and K. Zhou, "Numerical investigation of two-dimensional imaging for temperature and species concentration using tunable diode laser absorption spectroscopy," in *Proc. 2012 Int. Conf. Meas., Inf. Control*, 2012, vol. 1, pp. 234–238.
- [4] L. Ma *et al.*, "50-kHz-rate 2d imaging of temperature and H₂O concentration at the exhaust plane of a j85 engine using hyperspectral tomography," *Opt. Express*, vol. 21, no. 1, pp. 1152–1162, Jan. 2013. [Online]. Available: <http://www.opticsexpress.org/abstract.cfm?URI=oe-21-1-1152>
- [5] Z. Nadir, M. S. Brown, M. L. Comer, and C. A. Bouman, "Gaussian mixture prior models for imaging of flow cross sections from sparse hyperspectral measurements," in *Proc. 2015 IEEE Global Conf. Signal Inf. Process.*, Dec. 2015, pp. 527–531.
- [6] Z. Nadir, M. Brown, M. Comer, and C. Bouman, "Tomographic reconstruction of flowing gases using sparse training," in *Proc. 2014 IEEE Int. Conf. Image Process.*, Oct. 2014, pp. 1733–1737.
- [7] M. Arroyo and R. Hanson, "Absorption measurements of water-vapor concentration, temperature, and line-shape parameters using a tunable InGaAsP diode laser," *Appl. Opt.*, vol. 32, no. 30, pp. 6104–6116, 1993.
- [8] H. Semerjian and S. Ray, "Laser tomography for simultaneous concentration and temperature measurement in reacting flows," in *Proc. AIAA 18th Thermophys. Conf.*, Montreal, QC, Canada, 1983, pp. 300–324.
- [9] V. Kasyutich and P. Martin, "Towards a two-dimensional concentration and temperature laser absorption tomography sensor system," *Appl. Phys. B*, vol. 102, no. 1, pp. 149–162, 2011.
- [10] K. M. Busa, B. Rice, J. C. McDaniel, C. P. Goyne, R. D. Rockwell, J. A. Fulton, J. R. Edwards, and G. S. Diskin, "Direct measurement of combustion efficiency of a dual-mode Scramjet via TDLAT and SPIV," in *Proc. 53rd AIAA Aerosp. Sci. Meeting*, Jan. 2015, p. 0357.
- [11] P. Emmerman, R. Goulard, R. Santoro, and H. Semerjian, "Multiangular absorption diagnostics of a turbulent argon-methane jet," *J. Energy*, vol. 4, no. 2, pp. 70–77, 1980.
- [12] M. G. Allen, "Diode laser absorption sensors for gas-dynamic and combustion flows," *Meas. Sci. Technol.*, vol. 9, no. 4, pp. 545–562, 1998.
- [13] C. D. Lindstrom *et al.*, "Shock-train structure resolved with absorption spectroscopy, part I: System design and validation," *AIAA J.*, vol. 47, no. 10, pp. 2368–2378, 2009.
- [14] F.-Y. Zhang, T. Fujiwara, and K. Komurasaki, "Diode-laser tomography for arcjet plume reconstruction," *Appl. Opt.*, vol. 40, no. 6, pp. 957–964, 2001.
- [15] S. T. Sanders, J. Wang, J. B. Jeffries, and R. K. Hanson, "Diode-laser absorption sensor for line-of-sight gas temperature distributions," *Appl. Opt.*, vol. 40, no. 24, pp. 4404–4415, 2001.
- [16] X. Zhou, X. Liu, J. B. Jeffries, and R. Hanson, "Development of a sensor for temperature and water concentration in combustion gases using a single tunable diode laser," *Meas. Sci. Technol.*, vol. 14, no. 8, pp. 1459–1468, 2003.
- [17] C. Lindstrom, C.-J. Tam, D. Davis, D. Eklund, and S. Williams, "Diode laser absorption tomography of 2D supersonic flow," in *Proc. 43rd AIAA/ASME/SAE/ASEE Joint Propuls. Conf. Exhib.*, 2007, p. 5014.
- [18] R. Zhang, J.-B. Thibault, C. Bouman, K. Sauer, and J. Hsieh, "Model-based iterative reconstruction for dual-energy x-ray ct using a joint quadratic likelihood model," *IEEE Trans. Med. Imag.*, vol. 33, no. 1, pp. 117–134, Jan. 2014.
- [19] S. Venkatakrisnan, L. Drummy, M. Jackson, M. De Graef, J. Simons, and C. Bouman, "A model based iterative reconstruction algorithm for high angle annular dark field-scanning transmission electron microscope (HAADF-stem) tomography," *IEEE Trans. Image Process.*, vol. 22, no. 11, pp. 4532–4544, Nov. 2013.
- [20] A. C. Kak and M. Slaney, *Principles of Computerized Tomographic Imaging*, vol. 33. Philadelphia, PA, USA: SIAM, 1988.
- [21] J. Hsieh, *Computed Tomography: Principles, Design, Artifacts, and Recent Advances*. Bellingham, WA, USA: SPIE, 2009.
- [22] T. Palaghita and J. M. Seitzman, "Control of temperature nonuniformity based on line-of-sight absorption," in *Proc. 40th AIAA/ASME/SAE/ASEE Joint Propul. Conf. Exhib.*, 2004, Paper 4163.
- [23] C. Liu, L. Xu, and Z. Cao, "Measurement of axisymmetric temperature distributions using single view fan-beam TDLAS tomography," in *Proc. 2013 IEEE Int. Instrum. Meas. Technol. Conf.*, May 2013, pp. 876–879.
- [24] F. Wang *et al.*, "Two-dimensional tomography for gas concentration and temperature distributions based on tunable diode laser absorption spectroscopy," *Meas. Sci. Technol.*, vol. 21, no. 4, 2010, Art. no. 045301.

- [25] B. Hughey and D. Santavicca, "A comparison of techniques for reconstructing axisymmetric reacting flow fields from absorption measurements," *Combust. Sci. Technol.*, vol. 29, no. 3–6, pp. 167–190, 1982.
- [26] X. Liu, J. B. Jeffries, and R. K. Hanson, "Measurement of non-uniform temperature distributions using line-of-sight absorption spectroscopy," *AIAA J.*, vol. 45, no. 2, pp. 411–419, 2007.
- [27] J. Wang, M. Maiorov, J. B. Jeffries, D. Z. Garbuzov, J. C. Connolly, and R. K. Hanson, "A potential remote sensor of CO in vehicle exhausts using 2.3 μm diode lasers," *Meas. Sci. Technol.*, vol. 11, no. 11, pp. 1576–1584, 2000.
- [28] M. S. Brown, G. C. Herring, K. Cabell, N. Hass, T. F. Barhorst, and M. Gruber, "Optical measurements at the combustor exit of the HIFIRE 2 ground test engine," in *Proc. 50th AIAA Aerosp. Sci. Meeting Including New Horiz. Forum Aerosp. Expo.*, 2012, p. 857.
- [29] K. M. Busa, E. Ellison, B. McGovern, J. McDaniel, G. Diskin, M. DePiro, D. Capriotti, and R. Gaffney, "Measurements on NASA Langley durable combustor rig by TDLAT: preliminary results," in *Proc. 51st AIAA Aerosp. Sci. Meeting Including New Horiz. Forum Aerosp. Expo.*, 2013, p. 696.
- [30] R. Santoro, H. Semerjian, P. Emmerman, and R. Goulard, "Optical tomography for flow field diagnostics," *Int. J. Heat Mass Transfer*, vol. 24, no. 7, pp. 1139–1150, 1981.
- [31] M. Ravichandran and F. Gouldin, "Retrieval of asymmetric temperature and concentration profiles from a limited number of absorption measurements," *Combustion Sci. Technol.*, vol. 60, no. 1–3, pp. 231–248, 1988.
- [32] M. Ravichandran and F. C. Gouldin, "Reconstruction of smooth distributions from a limited number of projections," *Appl. Opt.*, vol. 27, no. 19, pp. 4084–4097, 1988.
- [33] L. Ma and W. Cai, "Numerical investigation of hyperspectral tomography for simultaneous temperature and concentration imaging," *Appl. Opt.*, vol. 47, no. 21, pp. 3751–3759, 2008.
- [34] W. Cai and L. Ma, "Hyperspectral tomography based on proper orthogonal decomposition as motivated by imaging diagnostics of unsteady reactive flows," *Appl. Opt.*, vol. 49, no. 4, pp. 601–610, 2010.
- [35] C. Bouman and K. Sauer, "A generalized gaussian image model for edge-preserving map estimation," *IEEE Trans. Image Process.*, vol. 2, no. 3, pp. 296–310, Jul. 1993.
- [36] K. Sauer and C. Bouman, "A local update strategy for iterative reconstruction from projections," *IEEE Trans. Signal Process.*, vol. 41, no. 2, pp. 534–548, Feb. 1993.
- [37] S. Venkatakrishnan, L. Drummy, M. Jackson, M. De Graef, J. Simmons, and C. Bouman, "A model based iterative reconstruction algorithm for high angle annular dark field-scanning transmission electron microscope (HAADF-stem) tomography," *IEEE Trans. Image Process.*, vol. 22, no. 11, pp. 4532–4544, Nov. 2013.
- [38] S. Ramani and J. A. Fessler, "A splitting-based iterative algorithm for accelerated statistical X-ray CT reconstruction," *IEEE Trans. Med. Imag.*, vol. 31, no. 3, pp. 677–688, Mar. 2012.
- [39] Z. H. Levine, A. J. Kearsley, and J. G. Hagedorn, "Bayesian tomography for projections with an arbitrary transmission function with an application in electron microscopy," *J. Res. Nat. Inst. Stand. Technol.*, vol. 111, no. 6, pp. 411–417, 2006.
- [40] C. Lindstrom, C.-J. Tam, R. Givens, D. Davis, and S. Williams, "Diode laser absorption tomography using data compression techniques," in *Proc. Electron. Imag.*, 2008, Paper 68 140W.
- [41] C. Bouman and K. Sauer, "A generalized gaussian image model for edge-preserving map estimation," *IEEE Trans. Image Process.*, vol. 2, no. 3, pp. 296–310, Jul. 1993.
- [42] J. Hsieh, C. A. Bouman, K. D. Sauer, and J.-B. Thibault, "A three-dimensional statistical approach to improved image quality for multislice helical CT," *Med. Phys.*, vol. 34, pp. 4526–4544, 2007.
- [43] J. Besag, "Spatial interaction and the statistical analysis of lattice systems," *J. Roy. Statist. Soc. B Methodological*, vol. 36, pp. 192–236, 1974.
- [44] T. Hebert and R. Leahy, "A generalized EM algorithm for 3-d Bayesian reconstruction from poisson data using Gibbs priors," *IEEE Trans. Med. Imag.*, vol. 8, no. 2, pp. 194–202, Jun. 1989.
- [45] S. S. Saquib, C. A. Bouman, and K. Sauer, "A non-homogeneous MRF model for multiresolution Bayesian estimation," in *Proc. Int. Conf. Image Process.*, 1996, vol. 1, pp. 445–448.
- [46] E. Haneda and C. Bouman, "Implicit priors for model-based inversion," in *Proc. 2012 IEEE Int. Conf. Acoust., Speech, Signal Process.*, Mar. 2012, pp. 3917–3920.
- [47] I. Cadez and P. Smyth, "Modeling of inhomogeneous Markov random fields with applications to cloud screening," Dept. Inf. Comput. Sci., Univ. California, California, Irvine, CA, USA, *Tech. Rep.*, Rep. no. 98–21, 1998.
- [48] A. Mehranian and H. Zaidi, "Joint estimation of activity and attenuation in whole-body TOF PET/MRI using constrained Gaussian mixture models," *IEEE Trans. Med. Imag.*, vol. 34, no. 9, pp. 1808–1821, Sep. 2015.
- [49] G. Wang, L. Schultz, and J. Qi, "Statistical image reconstruction for muon tomography using a Gaussian scale mixture model," *IEEE Trans. Nuclear Sci.*, vol. 56, no. 4, pp. 2480–2486, Aug. 2009.
- [50] L. S. Rothman *et al.*, "The Hitran 2004 molecular spectroscopic database," *J. Quant. Spectrosc. Radiative Transfer*, vol. 96, no. 2, pp. 139–204, 2005.
- [51] C. A. Bouman, "Cluster: An unsupervised algorithm for modeling Gaussian mixtures," Apr. 1997. [Online]. Available: <http://engineering.purdue.edu/bouman>
- [52] C. M. Bishop and N. M. Nasrabadi, *Pattern Recognition and Machine Learning*, vol. 1. New York, NY, USA: Springer-Verlag, 2006.
- [53] P. Kauranen, H. M. Hertz, and S. Svanberg, "Tomographic imaging of fluid flows by the use of two-tone frequency-modulation spectroscopy," *Opt. Lett.*, vol. 19, no. 18, pp. 1489–1491, 1994.
- [54] S. V. Venkatakrishnan, L. F. Drummy, M. Jackson, M. D. Graef, J. Simmons, and C. A. Bouman, "Model-based iterative reconstruction for bright-field electron tomography," *IEEE Trans. Comput. Imag.*, vol. 1, no. 1, pp. 1–15, Mar. 2015.
- [55] E. Haneda and C. Bouman, "Implicit priors for model based inversion," in *Proc. 2012 IEEE Int. Conf. Acoust., Speech Signal Process. (ICASSP)*, Mar. 2011, pp. 3917–3920, doi: 10.1109/ICASSP.2012.6288774.
- [56] R. Zhang, C. Bouman, J.-B. Thibault, and K. Sauer, "Gaussian mixture Markov random field for image denoising and reconstruction," in *Proc. 2013 IEEE Global Conf. Signal Inf. Process.*, Dec. 2013, pp. 1089–1092.
- [57] W. Enkelmann, "Investigations of multigrid algorithms for the estimation of optical flow fields in image sequences," *Comput. Vis., Graph. Image Process.*, vol. 43, no. 2, pp. 150–177, 1988.
- [58] E. Mémin and P. Pérez, "Dense estimation and object-based segmentation of the optical flow with robust techniques," *IEEE Trans. Image Process.*, vol. 7, no. 5, pp. 703–719, May 1998.
- [59] P. Saint-Marc, J.-S. Chen, and G. Medioni, "Adaptive smoothing: A general tool for early vision," *IEEE Trans. Pattern Anal. Mach. Intell.*, vol. 13, no. 6, pp. 514–529, Jun. 1991.
- [60] M. Unser, "Multigrid adaptive image processing," in *Proc. Int. Conf. Image Process.*, 1995, vol. 1, pp. 49–52.
- [61] D. L. Pham and J. L. Prince, "Adaptive fuzzy segmentation of magnetic resonance images," *IEEE Trans. Med. Imag.*, vol. 18, no. 9, pp. 737–752, Sep. 1999.
- [62] M. Arigovindan, M. Suhling, P. Hunziker, and M. Unser, "Multigrid image reconstruction from arbitrarily spaced samples," in *Proc. 2002 Int. Conf. Image Process.*, 2002, vol. 3, pp. III-381–III-384.
- [63] J. C. Ye, C. A. Bouman, K. J. Webb, and R. P. Millane, "Nonlinear multigrid algorithms for Bayesian optical diffusion tomography," *IEEE Trans. Image Process.*, vol. 10, no. 6, pp. 909–922, Jun. 2001.
- [64] S. Oh, A. B. Milstein, C. A. Bouman, and K. J. Webb, "A general framework for nonlinear multigrid inversion," *IEEE Trans. Image Process.*, vol. 14, no. 1, pp. 125–140, Jan. 2005.
- [65] W. H. Press, S. A. Teukolsky, W. T. Vetterling, and B. P. Flannery, *Numerical Recipes in C*, 2 ed. Cambridge, U.K.: Cambridge Univ. Press, 1996.
- [66] C. A. Bouman and K. Sauer, "A unified approach to statistical tomography using coordinate descent optimization," *IEEE Trans. Image Process.*, vol. 5, no. 3, pp. 480–492, Mar. 1996.
- [67] K. Sauer and C. Bouman, "A local update strategy for iterative reconstruction from projections," *IEEE Trans. Signal Process.*, vol. 41, no. 2, pp. 534–548, Feb. 1993.
- [68] J. Fischer, R. Gamache, A. Goldman, L. Rothman, and A. Perrin, "Total internal partition sums for molecular species in the 2000 edition of the hitran database," *J. Quant. Spectrosc. Radiative Transfer*, vol. 82, no. 1, pp. 401–412, 2003.



Zeeshan Nadir received the Bachelor's degree in electrical engineering in 2011 from the University of Engineering and Technology, Lahore, Pakistan, and the Master's degree in 2014 from Purdue University, West Lafayette, IN, USA, where he is currently working toward the Ph.D. degree in the School of Electrical and Computer Engineering. In Summer 2016, he was an intern at MathWorks, Inc., Natick, MA, USA, where he worked on MATLAB coder package. His research interests include statistical signal processing, inverse problems, computational imaging, machine

learning and computer vision.



Michael S. Brown received the Ph.D. degree in physics from The University of Texas at Austin, Austin, TX, USA, in 1989. He did his postdoctoral work in the Combustion Research Facility at Sandia National Laboratories where he designed and implemented advanced spectroscopy tools for combustion diagnostic applications. He spent eight years working in industry on applied laser-based diagnostic development before joining the Air Force Research Laboratory (AFRL) in 1999. Since then, he has been working on multiple research projects involving optical techniques aimed at a better understanding of engine behavior and performance. He is currently the Head of the Hypersonic Sciences Branch, AFRL.



Mary L. Comer (S'91–M'92–SM'96) received the B.S., M.S., and Ph.D. degrees from Purdue University, West Lafayette, IN, USA, in 1990, 1993, and 1995, respectively, all in electrical engineering. From 1992 until 1995, she held a National Science Foundation Graduate Fellowship. From 1995 to 2005, she was with Thomson, Indianapolis, IN, where she was a Senior Member of the Technical Staff in the Corporate Research Division. While at Thomson, she was involved with video coding, multiresolution video, and video postprocessing for applications, including high-definition DVD, Internet video, satellite television, and security and surveillance. She was a participant and contributor to the HD-DVD Forum committee tasked with recommending a video coding standard for high-definition video on red laser DVD discs. She served as the Demo Cochair for the 2007 IEEE International Symposium on Multimedia. She is currently an Associate Editor of the IEEE TRANSACTIONS ON CIRCUITS AND SYSTEMS FOR VIDEO TECHNOLOGY. She is currently an Associate Professor in the School of Electrical and Computer Engineering, Purdue University. Her research interests include statistical image modeling, texture-based segmentation of images, medical imaging, analysis of micro-structural images and multi-resolution/scalable video coding.



Charles A. Bouman (S'86–M'89–SM'97–F'01) received the B.S.E.E. degree from the University of Pennsylvania, Philadelphia, PA, USA, in 1981, and the M.S. degree from the University of California at Berkeley, Berkeley, CA, USA, in 1982. From 1982 to 1985, he was a full staff member at MIT Lincoln Laboratory and in 1989 he received a Ph.D. degree in electrical engineering from Princeton University, Princeton, NJ, USA. He joined the faculty of Purdue University in 1989 where he is currently the Showalter Professor of Electrical and Computer Engineering and Biomedical Engineering. He is the Codirector of Purdue's Magnetic Resonance Imaging Facility, Purdue Research Park. His research focuses on the use of statistical image models, multiscale techniques, and fast algorithms in applications including tomographic reconstruction, medical imaging, and document rendering and acquisition. He is a Fellow of the American Institute for Medical and Biological Engineering, a Fellow of the society for Imaging Science and Technology, and a Fellow of the SPIE Professional Society. He received the IS&T's Raymond C. Bowman Award for outstanding contributions to digital imaging education and research, has been a Purdue University Faculty Scholar, and received the College of Engineering Engagement/Service Award, and Team Award. He was previously the Editor-in-Chief of the IEEE TRANSACTIONS ON IMAGE PROCESSING and a Distinguished Lecturer for the IEEE Signal Processing Society, and he is currently a member of the Board of Governors. He has been an Associate Editor of the IEEE TRANSACTIONS ON IMAGE PROCESSING and the IEEE TRANSACTIONS ON PATTERN ANALYSIS AND MACHINE INTELLIGENCE. He has also been Cochair of the 2006 SPIE/IS&T Symposium on Electronic Imaging, Cochair of the SPIE/IS&T conferences on Visual Communications and Image Processing 2000, a Vice President of Publications and a member of the Board of Directors for the IS&T Society, and he is the founder and Cochair of the SPIE/IS&T Conference on Computational Imaging.